ELSEVIER

Dynamics of paramagnetic agents by off-resonance rotating frame technique

Huiming Zhang [a,b,*], Yang Xie [a]

[a] *Center for Basic MR Research, Evanston Northwestern Healthcare Research Institute, 1033 University Place, suite 100, Evanston, IL 60201, USA*
[b] *Department of Radiology, Feinberg Medical School of Northwestern University, Chicago, IL 60611, USA*

Abstract

Off-resonance rotating frame technique offers a novel tool to explore the dynamics of paramagnetic agents at high magnetic fields ($B_0 > 3$ T). Based on the effect of paramagnetic relaxation enhancement in the off-resonance rotating frame, a new method is described here for determining the dynamics of paramagnetic ion chelates from the residual z-magnetizations of water protons. In this method, the dynamics of the chelates are identified by the difference magnetization profiles, which are the subtraction of the residual z-magnetization as a function of frequency offset obtained at two sets of RF amplitude ω_1 and pulse duration τ. The choices of ω_1 and τ are guided by a 2-D magnetization map that is created numerically by plotting the residual z-magnetization as a function of effective field angle θ and off-resonance pulse duration τ. From the region of magnetization map that is the most sensitive to the alteration of the paramagnetic relaxation enhancement efficiency $R_{1\rho}/R_1$, the ratio of the off-resonance rotating frame relaxation rate constant $R_{1\rho}$ verse the laboratory frame relaxation rate constant R_1, three types of difference magnetization profiles can be generated. The magnetization map and the difference magnetization profiles are correlated with the rotational correlation time τ_R of Gd-DTPA through numerical simulations, and further validated by the experimental data for a series of macromolecule conjugated Gd-DTPA in aqueous solutions. Effects of hydration water number q, diffusion coefficient D, magnetic field strength B_0 and multiple rotational correlation times are explored with the simulations of the magnetization map. This method not only provides a simple and reliable approach to determine the dynamics of paramagnetic labeling of molecular/cellular events at high magnetic fields, but also a new strategy for spectral editing in NMR/MRI based on the dynamics of paramagnetic labeling *in vivo*.
© 2006 Elsevier Inc. All rights reserved.

Keywords: Off-resonance rotating frame; Paramagnetic relaxation enhancement; Magnetization map; Magnetization profiles; Difference magnetization profiles; Dynamic of paramagnetic chelates

1. Introduction

The relaxivity of macromolecule conjugated paramagnetic ion chelates contains the dynamic information of the magnetic unit itself. Their relevant motional correlation times can be extracted from NMR dispersion profiles measured by field cycling spectrometers, in which the proton Larmor frequency is swept from 0.01 kHz to 30 MHz [1,2]. Previous studies have shown that the relaxivity for the chelates containing the paramagnetic ions such as Mn(II) or Gd(III) is a function of magnetic field strength with a maximum located at ~20 MHz of proton Larmor frequency [3]. The amplitude of this maximum depends on the effective motional correlation time τ_c. This technique has been used extensively for studying the dynamics of biological systems through paramagnetic labeling [4]. However, the relaxivity decreases rapidly as the magnetic field is higher than 3 T due to the frequency dependence of the relaxivity [5]. Consequently, all dynamic differences between the paramagnetic agents disappear at the field strength $\omega_{H,S}\tau_c \gg 1$ and the spectral density function $J(\omega_{H,S}) \to 0$, where $\omega_{H,S}$ is the Larmor frequency for

---
* Corresponding author. Fax: +1 847 492 0731.
E-mail address: h-zhang1@northwestern.edu (H. Zhang).

electron (S) and for proton (H). Since the dynamics of paramagnetic labeling can be correlated with its function involved in molecular/cellular events [6], the low relaxivity at high magnetic fields ($B_0 > 3T$) prevents it from differentiating the dynamics of paramagnetic labeling at high magnetic fields.

We have shown in the previous paper that the frequency dependence of the spectral density function can be altered by transferring from laboratory frame to off-resonance rotating frame for the ^1H spin that is dipolarly coupled to an electron [7]. As the results, the relaxivity at high magnetic fields is enhanced. The off-resonance rotating frame is achieved by a long off-resonance pulse as shown in the previous paper [7], which is also a routine sequence used in NMR/MRI for spin saturations or magnetization transfer (MT) [8,9], and for the spin relaxations in the off-resonance rotating frame [10–14]. This sequence contains a long off-resonance pulse with duration τ and RF amplitude ω_1 irradiated at frequency offset Δ. Under the RF irradiation, the spins are tilted to a θ angle, $\theta = tg^{-1}(\omega_1/\Delta)$. By the end of the long pulse, a following 90° pulse reads out the residual z-magnetizations. In this method, the relaxation rate of water protons depends primarily on the effective field strength of the off-resonance rotating frame ω_e and partially on the magnetic field strength ω_H. The relaxivity is enhanced by a factor defined as paramagnetic relaxation enhancement efficiency $R_{1\rho}/R_1$ [7], the ratio of the off-resonance rotating frame relaxation rate constant $R_{1\rho}$ verse the laboratory frame relaxation rate constant R_1, which is a function of $(\omega_H\tau_c)^2$. Thus, the dynamics of paramagnetic agents at high magnetic fields can be differentiated by measuring the residual z-magnetization of water protons in the off-resonance rotating frame.

Methods for correlating the residual z-magnetizations of off-resonance rotating frame with the molecular dynamics have been known since 1970s [10–14]. In these studies, spins such as ^{13}C were used to label the sites so that their residual z-magnetizations directly reflected the dynamics of the molecule at where they were attached. Then, the extraction of the dynamic parameters were carried out by analysis of the residual z-magnetization dispersion profiles, which is the residual z-magnetization plotted as a function of frequency offset at fixed RF amplitude. Since the distribution of the equilibrium residual z-magnetization profiles is directly related to the rotating frame relaxation rate constants, thus the dynamic parameters are determined by fitting the profiles with specific kinetic models [10–14]. This method can effectively detect the spins in the motional scale of ps-μs.

Exploring the dynamics of paramagnetic agents by the off-resonance rotating frame technique is different. In the case of paramagnetic ion chelates, their dynamic parameters are explicitly expressed in the magnetization of water protons via the special kinetic models, namely the inner shell water model (IS) and outer shell water model (OS), which have been known for many years [4,15–18]. The detection of the dynamics of the paramagnetic agents will

be carried out through the residual z-magnetization of water protons based on the effect of paramagnetic relaxation enhancement in the off-resonance rotating frame. Our previous paper has presented a comprehensive relaxation theory for paramagnetic agents in off-resonance rotating frame, which included the contributions from the inner shell and the outer shell water [7]. The derived formalisms for the relaxation rate constants contain several structural and dynamic parameters such as the number of coordinated water q, the effective motional correlation time τ_c for the inner shell water and the effective diffusion correlation time τ_D for the outer shell water. Since multiple parameters are related to the relaxation rate constants, tedious procedure for data fitting will be needed for the extraction of these parameters.

The motivation of present work was to establish a simple method to identify the dynamics of paramagnetic ion chelates by the characteristics of their residual z-magnetization profiles. This is only possible if the residual z-magnetization profiles are acquired in such way that their characteristics are directly correlated with the dynamics, and the pattern of the profiles can be easily recognized by comparing with the standards. Such method will not only simplify the tedious procedure for data processing, but also offers a novel protocol for *in vivo* applications. Thus, the dynamics of paramagnetic labeling can be used to follow the progress of molecular/cellular events.

In this work, we present a new method for determining dynamics of paramagnetic ion chelates via the residual z-magnetization of water protons in off-resonance rotating frame. For the simplicity, we only consider the paramagnetic contribution to the proton spin relaxation in aqueous solutions in which the MT contribution can be neglected. The diamagnetic contribution also can be neglected because the paramagnetic contribution is dominant. Starting with the motional equation of magnetization in the rotating frame, the derived residual z-magnetization $M_e(\tau, \theta)$ is expressed as a function of the rotating frame spin–lattice relaxation rate constant $R_{1\rho}$ and the paramagnetic relaxation enhancement efficiency $R_{1\rho}/R_1$. By plotting $M_e(\tau, \theta)$ verse θ for all τ, a magnetization map is created. From the region of magnetization map that is the most sensitive to the alteration of paramagnetic relaxation enhancement efficiency $R_{1\rho}/R_1$, three types of difference magnetization profiles are generated. The magnetization map and the difference magnetization profiles are correlated with the rotational correlation time τ_R of Gd-DTPA through numerical simulations, and further validated by the experimental data for a series of macromolecule conjugated Gd-DTPA in aqueous solutions. Effects of coordinated water number q, diffusion coefficient D, magnetic field strength B_0 and multiple rotational correlation times are explored with the simulations of the magnetization map.

The presence of the MT effects *in vivo* will add additional complicating factors to the case of paramagnetic ion chelates in solutions. We have quantitatively analyzed the spin relaxations for the paramagnetic ion chelates in the

presence of strong MT effects by theoretical simulations and experimental verifications. This latest progress will be presented in details in a separate paper later, which will demonstrate the method presented here is a powerful tool for the data analysis *in vivo*.

2. Method

For the aqueous solution containing paramagnetic ion chelates in the region of $(R_{1,1\rho})_{\text{diamag}} \ll (R_{1,1\rho})_{\text{paramag}}$, we consider the transient response of water proton spins to the off-resonance long pulse. During this pulse period, the magnetization is the contribution sum of paramagnetic relaxation pathway and other spin relaxation pathways such as magnetization transfer and diffusion exchange. For paramagnetic agents in aqueous media, if the contributions from other relaxation pathways can be neglected, we only need to consider the contribution from the paramagnetic relaxation pathway. Including the contributions from other relaxation pathways will complicate the analysis, as we will show in a successive paper in details for systems that have contributions from magnetization transfer pathway.

Assuming that the magnetization for the paramagnetic relaxation pathway decays in the effective field as a single exponential function of τ, the motion equation of the residual z-magnetization $M_e(\theta)$ at the effective field angle θ is as follows:

$$dM_e(\theta)/d\tau = -R_{1\rho}(\theta)M_e(\theta). \quad (1)$$

where the residual z-magnetization $M_e(\theta)$ differs from the rotating frame magnetization M_e by a factor of $\cos\theta$, $M_e(\theta) = M_e \cos\theta$. From Eq. (1), the residual z-magnetization $M_e(\theta)$ as a function of pulse duration τ is derived as

$$M_e(\tau, \theta) = A \exp(-R_{1\rho}(\theta)\tau) + C, \quad (2)$$

where A and C are θ-dependent constants and are defined by the initial magnetization $M_e(0_+, \theta)$ and the equilibrium residual z-magnetization $M_e(\infty, \theta)$. Since $M_e = M_0 \cos\theta$ and $M_e(\infty) = M_e R_1/R_{1\rho}$ in general [10,11], the residual z-magnetizations at $\tau = 0_+$ and $\tau = \infty$ are as follows:

$$M_e(0_+, \theta) = M_0 \cos^2\theta, \quad (3)$$

$$M_e(\infty, \theta) = M_0 \cos^2\theta \frac{R_1}{R_{1\rho}(\theta)}. \quad (4)$$

Thus, Eq. (2) can be expressed as,

$$M_e(\tau, \theta) = M_0 \cos^2\theta$$
$$\times \left\{ \left(1 - \frac{R_1}{R_{1\rho}(\theta)}\right) \exp(-R_{1\rho}(\theta)\tau) + \frac{R_1}{R_{1\rho}(\theta)} \right\} \quad (5)$$

with

$$R_1 = R_1^{\text{IS}} + sR_1^{\text{OS}} \quad (6)$$
$$R_{1\rho}(\theta) = R_{1\rho}^{\text{IS}}(\theta) + sR_{1\rho}^{\text{OS}}(\theta) \quad (7)$$

where s is the space assessable coefficient for the outer shell water of macromolecule conjugated paramagnetic ion chelates [7]. R_1^{IS}, R_1^{OS} are the laboratory spin–lattice relaxation rate constants for the inner shell water (IS) and the outer shell water (OS) respectively. $R_1^{\text{IS}}(\theta)$, $R_1^{\text{OS}}(\theta)$ are the rotating frame spin–lattice relaxation rate constants, their formalisms are provided in the appendix. R_1 and $R_{1\rho}(\theta)$ are the total spin–lattice relaxation rate constants for the laboratory frame and the rotating frame respectively. According to Eq. (4), the equilibrium residual z-magnetization $M_e(\infty, \theta)$ can solely define the relaxation enhancement efficiency $R_{1\rho}(\theta)/R_1$. In order to obtain the dynamic parameters of paramagnetic ion chelates, both $R_{1\rho}(\theta)$ and $R_{1\rho}(\theta)/R_1$ are required according to our previous work [7]. But $R_{1\rho}(\theta)$ only can be determined by the transient magnetization $M_e(\tau, \theta)$, as indicated by Eq. (5).

Eq. (5) can be used to calculate $M_e(\tau, \theta)$ for all θ and τ. A magnetization map is generated by plotting the residual magnetization $M_e(\tau, \theta)$ as a function of θ and τ. Fig. 1 shows the magnetization map for paramagnetic ion chelates with the relaxation enhancement efficiency $R_{1\rho}/R_1 > 1$. In this magnetization map, $M_e(0_+, \theta)$ defines the upper limit and $M_e(\infty, \theta)$ determines the lower limit. The transient residual z-magnetization $M_e(\tau, \theta)$ has the amplitude between the two limits, $M_e(0_+, \theta) > M_e(\tau, \theta) > M_e(\infty, \theta)$. Since $M_e(\tau, \theta)$ and $M_e(\infty, \theta)$ are determined by $R_{1\rho}(\theta)$ and $R_{1\rho}(\theta)/R_1$, the shape of the magnetization thus reflects the influence of paramagnetic agent's dynamics. The difference between the magnetization $M_e(0_+, \theta)$ and $M_e(\infty, \theta)$ is as follows:

$$\Delta M_e(\theta) = M_e(0_+, \theta) - M_e(\infty, \theta)$$
$$= M_e(0_+, \theta)\left[1 - \frac{1}{R_{1\rho}(\theta)/R_1}\right] \quad (8)$$
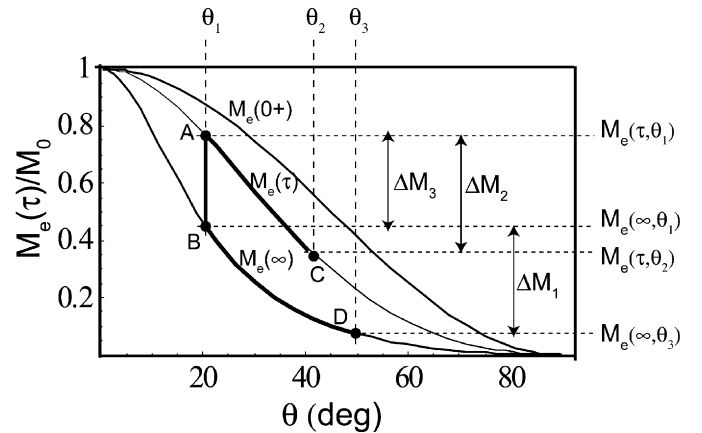

Fig. 1. Schematic illustration of magnetization map in off-resonance rotating frame. For the map, $M_e(0_+)$ defines the upper limit and $M_e(\infty)$ defines the lower limit. A, B, C and D are the labels for the magnetization $M_e(\tau, \theta)$ selected arbitrarily, where A denotes for $M_e(\tau, \theta_1)$, B denotes for $M_e(\infty, \theta_1)$, C denotes for $M_e(\tau, \theta_2)$ and D denotes for $M_e(\infty, \theta_3)$. The dark black lines represent the path for generating the difference magnetization. Three types of difference magnetization profiles can be generated: type-1 is defined by the path BD, $\Delta M_1 = M_e(\infty, \theta_1) - M_e(\infty, \theta_3)$; type-2 is defined by the path AC, $\Delta M_2 = M_e(\tau, \theta_1) - M_e(\tau, \theta_2)$; and type-3 is defined by the path AB, $\Delta M_3 = M_e(\tau, \theta_1) - M_e(\infty, \theta_1)$.

Eq. (8) defines the dynamic range $\Delta M_e(\theta)$ for the magnetization map, which is a function of the initial residual z-magnetization $M_e(0_+, \theta)$ and the relaxation enhancement efficiency $R_{1\rho}(\theta)/R_1$. The initial magnetization $M_e(0_+, \theta)$ at $\theta \to 90°$ is near to zero, where no detectable residual z-magnetization remains even through $R_{1\rho}(\theta)/R_1$ is at the maximum. On the other hand, no significant change of the residual z-magnetization can be defined at $\theta \to 0$, where the large initial magnetization $M_e(0_+, \theta)$ meets with small relaxation enhancement effect, $R_{1\rho}(\theta)/R_1 \sim 1$. So the maximum dynamic range of the magnetization map is located at $\theta \sim 45°$ due to the combination effect of $M_e(0_+, \theta)$ and $R_{1\rho}(\theta)/R_1$. The difference of the residual z-magnetization $\Delta M_e(\theta)$ at this angle is very sensitive to any alterations of the relaxation enhancement efficiency $R_{1\rho}(\theta)/R_1$. Thus, the magnetization difference nearby this angle can be used for examining the dynamics of paramagnetic ion chelates. Away from this angle, the dynamic range gradually reduces to zero.

The magnetization map provides a comprehensive picture to visualize all the residual z-magnetizations in the off-resonance rotating frame. Since many θ angles cannot be achieved experimentally, this map is generated only by theoretical calculations. Experimentally, magnetization profiles can be determined by varying frequency offset at fixed RF amplitude. The magnetization map can provide guidance for generating certain types of magnetization profiles with distinguishable characteristics. Because the shape of magnetization map is determined by the enhancement efficiency $R_{1\rho}(\theta)/R_1$, the magnetization profiles need to be chosen in such way that their distribution patterns can be used to identify the dynamics directly. Based on the relationship between the dynamics range of the magnetization map with the relaxation enhancement efficiency, the difference in magnetization is suitable for this purpose.

In Fig. 1, A, B, C and D are the labels for the magnetization $M_e(\tau, \theta)$, where A denotes for $M_e(\tau, \theta_1)$, B denotes for $M_e(\infty, \theta_1)$, C denotes for $M_e(\tau, \theta_2)$ and D denotes for $M_e(\infty, \theta_3)$. Here the choice of ABCD is arbitrary for the demo purpose. The solid dark line connects the labeling in pairs, i.e., AB, AC and BD. Each of the pairs represents a specific path for the difference magnetization. BD defines the equilibrium magnetization of different θ angle; AB defines the transient magnetization of different pulse duration and AC defines the transient magnetization of different θ angle. Thus, three types of difference magnetization profiles can be generated. Type-1 is defined by the path BD, $\Delta M_1 = M_e(\infty, \theta_1) - M_e(\infty, \theta_3)$, which is obtained by using different RF amplitudes to measure equilibrium magnetizations. Type-2 is defined by the path AC, $\Delta M_2 = M_e(\tau, \theta_1) - M_e(\tau, \theta_2)$. Type-3 is defined by the path AB, $\Delta M_2 = M_e(\tau, \theta_1) - M_e(\infty, \theta_1)$.

Each type of the difference magnetization profiles has its unique features. The type-1 difference magnetization profiles correspond to the equilibrium magnetization and can be used to determine $R_{1\rho}(\theta)/R_1$ directly. The type-2 difference magnetization profiles and the type-3 difference

magnetization profiles are the transient difference magnetizations that are a function of $R_{1\rho}(\theta)$ and $R_{1\rho}(\theta)/R_1$. Any one of them can be used for qualitatively differentiating the dynamics of paramagnetic ion chelates. However, in order to quantitatively determine the contributions of the inner shell water and the outer shell water, the type-1 combining with the type-2 or the type-3 are needed. Experimentally, the three types are measured with different sets of RF parameters, which provides the flexibility for instrument hardware and pulse sequence parameters. Such flexibility is essentially important for *in vivo* applications, where the RF amplitude or the pulse duration is limited by the specific absorption rate SAR set by FDA [19].

Due to the unique connection between the magnetization map and the corresponding difference magnetization profiles, the magnetization map is the starting point for any dynamics study and the guidance for selections of RF pulse parameters experimentally. This will be demonstrated in the numerical simulations for the Gd-DTPAs of different dynamics and the measurements of difference magnetization profiles for a series of macromolecule conjugated Gd-DTPA of known dynamics at 9.4T.

2.1. Numerical simulations

Calculations of magnetizations were performed for macromolecule conjugated Gd-DTPA. The parameters used in the calculations are same as those in our previous paper [7] and can be found elsewhere [5,20,21]. They are: $S = 7/2$, $q = 1$–3, $\tau_v = 38$ ps, $\tau_{s0} = 85$ ps, $\tau_m = 0.244$ µs, $r = 3.05$ Å, $\tau_R = 80$, 1500 and 3000 ps, $d = 3.6$ Å, $D = 3.16 \times 10^{-5}$ and 1.0×10^{-6}, $s = 0.75$, $c_{Gd} = 1$ mM [7]. In this list, S is the electron spin number, q is the number of water molecular bound per metal ion, τ_v is the correlation time characterized the fluctuation of the zero field splitting (ZFS), τ_{s0} is related to ZFS constant B as $\tau_{s0} = \tau_v/5B$, τ_m is the residual time of structural water, r is the electron-proton distance, τ_R is the rotational correlation time, d is the distance of closest approach of the water molecule to the metal complex, D is the sum of the diffusion coefficients of water molecule (D_I) and metal ion complex (D_S), S is the space assessable coefficient for the outer shell water for macromolecule conjugated paramagnetic ions, c_{Gd} is the gadolinium concentration. RF amplitude ω_1 is 2, 4 and 6 kHz, and offset Δ varies from 5 kHz to 60 kHz. All calculations were performed with Mathematica software.

3. Experimental

3.1. Synthesis of paramagnetic agents

Bovine serum albumin (BSA, M_w 68 kDa) from Aldrich was dissolved in 0.1 M Hepes buffer at pH 7.4, an excess dianhydride c-DTPA was added in 5 equal portions during 1 h at room temperature [22]. The solution was stirred for 1 h and then passed through a 0.2 µm filter. In an ice bath, equal mole of $GdCl_3$ to DTPA was added into the filtrate

in 5 equal portions during 1 h at pH 6.0. The solution was stirred for 24 h at 4 °C, and Arsenazo III was used to test free Gd^{3+} ion [23]. The solution was centrifuged with Amicon Ultra-15 from Millipore with molecular weight cutoff (MWCO) of 5 kDa, and lyophilized to a white solid powder. The product was analyzed for protein concentration by UV absorbency at 595 nm with Bradford assay and for gadolinium content by atomic emission spectroscopy (AES). The averaged molecular formula is $(Gd-DTPA)_{30}$-BSA by using a 200-fold excess dianhydride c-DTPA or is $(Gd-DTPA)_6$-BSA by using a 50-fold excess dianhydride c-DTPA in the synthesis

Polylysine (PLS, M_w 15–30 kDa) from Aldrich was dissolved in 0.1 M sodium bicarbonate buffer at pH 9.0, a 60-fold excess dianhydride c-DTPA was added in 5 equal portions during 1 hour at ice bath [22]. This mixture was warmed up to room temperature and stirred for six hours. A small portion of the resulting solution containing PLS-DTPA was purified for structure analysis. A colorimetric assay was used to determine the binding percentage of DTPA. The rest portion was reacted with $GdCl_3$ for six hours and Arsenazo III was used to test free Gd^{3+} ion. The solution was centrifuged with Amicon Ultra-15 from Millipore (Billerica, MA) with molecular weight cutoff (MWCO) of 5 kDa and lyophilized to a white solid powder. The averaged molecular formula of the contrast agent is $(Gd-DTPA)_{54}$-PLS.

Dextran (M_w 15–20 kDa) from Fluka, dried overnight at 70 °C, was reacted with DTPA dianhydride at a ratio of 1 DTPA per 2 glucose units in dry DMSO at 60 °C for 30 min [24]. After adding water and adjusting pH to 6, $GdCl_3$ based on 1:1 mole ratio to DTPA was added and allowed to react for 5 h. Free Gd^{3+} test was negative with Arsenzo III. The resulting solution was ultra-filtrated by Amicon Ultra-15 and lyophilized. The mole ratio of DTPA to dextran was determined by elemental analysis. The averaged molecular formula of the contrast agent was found to be $(Gd-DTPA)_8$-dextran.

1% PAMAM dendrimer-g5 (M_w 28.8 kDa) from Sigma–Aldrich was mixed with 45-fold excess p-SCN-benzyl-DTPA (Macrocyclics, Hoston, TX) [25]. The mixed solution was adjusted to pH 9 and maintained temperature at 40 °C for 24 h. $GdCl_3$ was added into the solution and stirred for 5–6 h. Free Gd^{3+} test was negative with Arsenzo III. The resulting solution was ultra-filtrated by Amicon Ultra-15 and lyophilized. The mole ratio of DTPA to PAMAM was determined by elemental analysis. The molecular formula of the contrast agent is $(Gd-DTPA-SCN-Bz)_{41}$-PAMAM-g5.

3.2. NMR measurements

All NMR experiments were carried with volume coils on a 4.7 T Bruker Biospec imaging spectrometer and a 9.4 T Bruker Advance micro-imaging spectrometer. Samples at 1 mM gadolinium concentration were placed in a 5 mm tube in a Bruker ^1H 10 mm resonator at room temperature

for the 9.4 T, or a 0.2 ml plastic vial placed in a homebuilt ^1H volume coil with 2 cm O.D. for the 4.7 T. The off-resonance rotating frame magnetization profiles were obtained by applying a long pulse with a 5–60 kHz frequency offset followed by a 90° reading pulse. The residual z-magnetization was plotted as a function of offset frequency to generate the magnetization profiles. Their fitted curves were used to generate the difference magnetization profiles. The off-resonance pulses were 500 ms long with RF amplitudes of 2, 4 and 6 kHz, the width of 90° pulse was 30 μs and the relaxation delay was 20 s.

4. Results and discussions

4.1. Magnetization map and various rotating frame magnetization profiles

Fig. 2 demonstrates the theoretically predicted magnetization map and various rotating frame magnetization profiles as a function of τ_R, which can be used to establish the connection between the magnetization map and various magnetization profiles. This figure contains the magnetization map shown in Fig. 2(A), the equilibrium residual z-magnetization profiles shown in Fig. 2(B), the type-1 difference magnetization profiles shown in Fig. 2(C), the type-2 difference magnetization profiles shown in Fig. 2(D) and the type-3 difference magnetization profiles shown in Fig. 2(E) for Gd-DTPA with $\tau_R = 80$, 1500 and 3000 ps, $q = 1$ and $D = 3.16 \times 10^{-5}$ cm²/s at 9.4 T.

Fig. 2(A) shows the theoretically predicted magnetization maps. These calculated residual z-magnetizations only include the paramagnetic contribution. In order to correlate the magnetization map with the residual z-magnetization profiles, the magnetization dispersion profiles and three types of difference magnetization profiles are also illustrated in the Fig. 2. At high fields, the effective motional correlation time τ_c is determined by the rotational correlation time τ_R ($\tau_c \sim \tau_R$). The inner shell relaxation rate constant $R_{1\rho}^{IS}(\theta)$, which is directly proportional to τ_R^2, will be much larger than the outer shell relaxation rate constant $R_{1\rho}^{OS}(\theta)$ at $\tau_R \geqslant 1500$ ps [7]. As results, the total relaxation rate constant $R_{1\rho}(\theta)$ is dominated by the inner shell relaxation rate constant $R_{1\rho}^{IS}(\theta)$ and the relaxation enhancement efficiency $R_{1\rho}(\theta)/R_1 \gg 1$. According to Eq. (8), the dynamic range of the magnetization map $M_e(0_+, \theta) - M_e(\infty, \theta)$ is a function of $\{1 - 1/(R_{1\rho}(\theta)/R_1)\}$, thus is expected to increase as τ_R increases from 80 to 3000 ps. Because $R_{1\rho}(\theta)$ is directly proportional to τ_R^2, the $\exp(-R_{1\rho}(\theta)\tau)$ term in Eq. (5) will make the transient magnetization $M_e(\tau, \theta)$ to decay faster at larger τ_R. Consequently, the difference transient magnetization $\{M_e(0_+, \theta) - M_e(\tau, \theta)\}$ also increases as τ_R increases from 80 to 3000 ps. Therefore, if τ_R of the paramagnetic ion chelates is very large, a pulse with short duration τ is capable to induce sufficiently large magnetization difference. This will benefit in vivo applications in which the RF power deposition on subjects can be reduced accordingly.
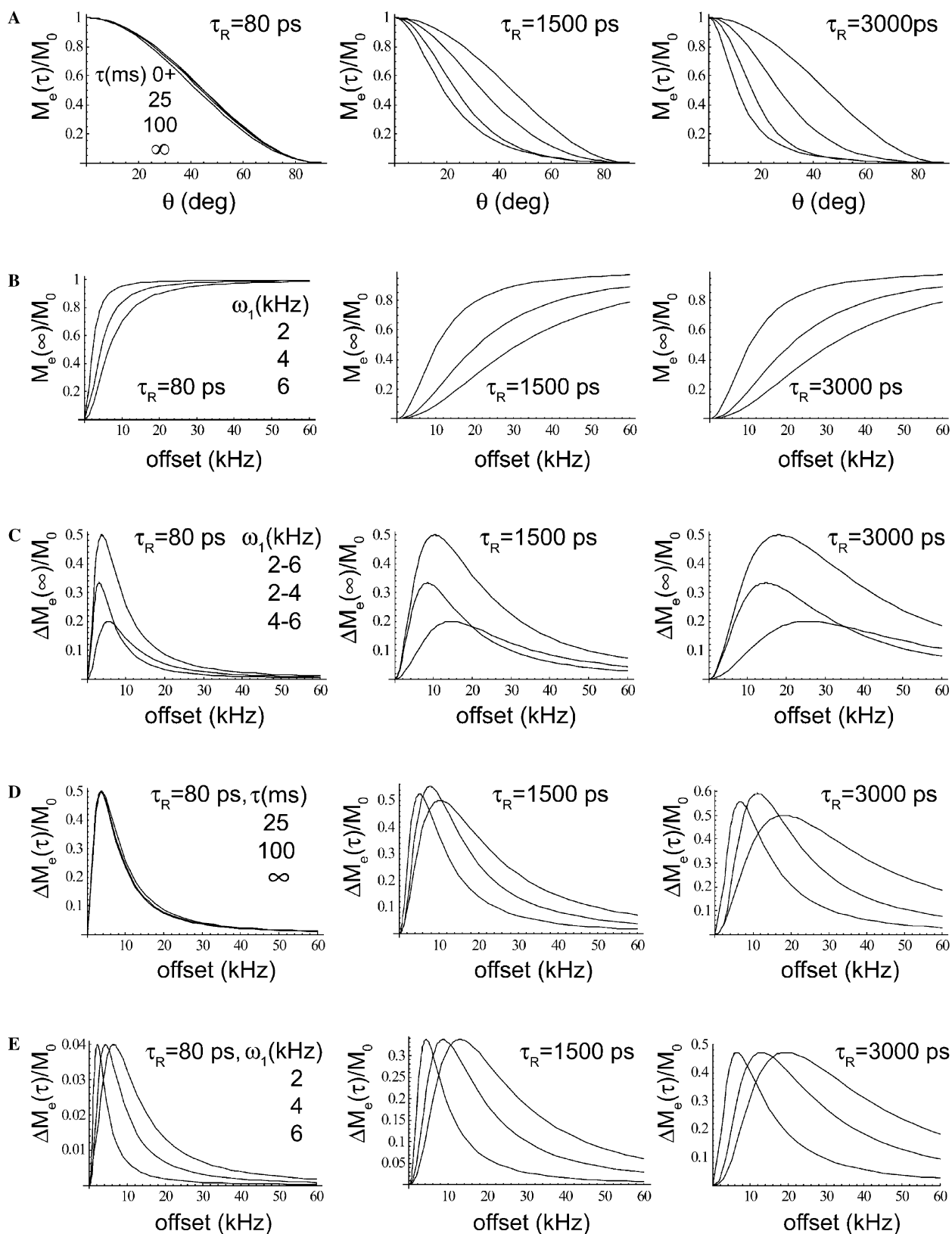
Fig. 2. Theoretically predicted magnetization maps and various magnetization profiles for paramagnetic chelates in aqueous solutions at 9.4 T. These maps and profiles are corresponding to the rotational correlation time τ_R of 80–3000 ps. Molecular parameters are discussed in the text. (A) Magnetization maps. (B) Equilibrium residual z-magnetization profiles with RF amplitude of 2, 4 and 6 kHz, the profile with a larger dispersion corresponds to the higher RF amplitude. (C) Type-1 difference magnetization profiles, $\Delta M_{1,2-6}$, $\Delta M_{1,2-4}$ and $\Delta M_{1,4-6}$. (D) Type-2 difference magnetization profiles $\Delta M_{2,2-6}(\tau_i)$ with $\tau_i = 25$, 100 ms and ∞, the maximum of the profiles shifts to higher offset as the pulse duration τ_i increases. (E) Type-3 difference magnetization profiles $\Delta M_{3,\omega_i}$ with $\omega_i = 2$, 4 and 6 kHz, the maximum of the profiles shifts to higher offset as the RF amplitude ω_i increases.

Fig. 2(B) shows the equilibrium residual z-magnetization profiles obtained at three RF amplitudes, with the same structural and dynamic parameters as those used for the Fig. 2(A) calculations. The profile with the lower intensity was acquired with the larger RF amplitude ω_1. All these profiles have a dispersion at the low offset region ($\Delta < 30$ kHz). This dispersion is the feature to be related to the magnetization map. Both the dispersion and the magnetization map can be altered by the same dynamic parameters such as the τ_R. As shown in Fig. 2(A and B), a large τ_R yields a wide dynamic range of the magnetization map and a large dispersion of the profiles. The dispersion is also a function of applied RF amplitude because the change of RF amplitude corresponds to the change of θ angle. Examples as when the RF amplitude steps up from 2 kHz to 6 kHz at 5 kHz frequency offset, it is equivalent to increase θ angle from 22° to 50°. $R_{1\rho}(\theta)$ will increase as the θ angle increases, which enhance the dispersion in the residual z-magnetization profile.

Fig. 2(C) shows the type-1 difference magnetization profiles defined by Fig. 1. Equilibrium magnetization profiles are obtained at RF amplitude of 2, 4 and 6 kHz, their corresponding effective angle is θ_1, θ_2 and θ_3, respectively. By subtraction, three difference profiles are generated as $\Delta M_{1,2-6} = M_e(\tau, \theta_1) - M_e(\tau, \theta_3)$, $\Delta M_{1,2-4} = M_e(\tau, \theta_1) - M_e(\tau, \theta_3)$, and $\Delta M_{1,4-6} = M_e(\infty, \theta_2) - M_e(\infty, \theta_3)$. The subscript 1 represents the type-1 difference magnetization profile, 2–6 denotes the magnetization difference between ω_1 of 2 and 6 kHz, 2–4 denotes the magnetization difference between ω_1 of 2 and 4 kHz, and 4–6 denotes the magnetization difference between ω_1 of 4 and 6 kHz. These notations will be used throughout the rest of paper. Each of the difference magnetization profiles shows a broad distribution with a maximum located at the low frequency offset. $\Delta M_{1,2-6}$ has the largest amplitude, $\Delta M_{1,2-4}$ has the narrowest distribution width, $\Delta M_{1,4-6}$ has the lowest amplitude and the broadest width. The frequency offsets for these maxima are in the order of $\Delta M_{1,2-4} < \Delta M_{1,2-6} < \Delta M_{1,4-6}$. As τ_R increases from 80 to 3000 ps, all three difference magnetization profiles shift to higher frequency offset and become broader. But the amplitude for each maximum is about the same. The connection of these difference magnetization profiles with the magnetization map can be defined by the position and width of the maximum. A larger dynamic range in the magnetization map corresponds to a broader distribution at higher frequency offset. This type of difference magnetization profiles defines the largest difference of magnetization for paramagnetic ion chelates.

Fig. 2(D) shows the type-2 difference magnetization profiles defined by Fig. 1. Transient magnetization profiles are obtained at RF amplitude of 2 and 6 kHz with pulse duration of 25 ms, 100 ms and ∞. The maxima of these magnetization profiles shift to higher frequency offset as the pulse duration increases. By subtraction, three difference magnetization profiles are generated as are $\Delta M_{2,2-6}(\tau_i) = M_e(\tau_i, \theta_1) - M_e(\tau_i, \theta_3)$ with $\tau_i = 0.025$ s, 0.1 s and ∞. The subscript 2 denotes the type-2 difference magnetization

profiles and 2–6 denotes the magnetization difference between ω_1 of 2 and 6 kHz. In this type of difference magnetization profile, the increase of τ means that the spins are closer to the equilibrium status. For $\tau_R \sim 80$ ps, there is no difference between the three difference magnetization profiles. This is expected since its magnetization map shows nearly zero dynamic range. For $\tau_R \sim 3000$ ps, there is a very large dynamic range in the magnetization map. As the pulse duration τ increases, the maximum of the profile shifts to higher offset and becomes very broader, but the amplitude of the maximum decreases only 10–15%. The offset change and the width change are a function of τ_R, i.e., the changes in frequency offset and width for 1500 ps τ_R are less than those for 3000 ps τ_R. The connection of these difference magnetization profiles with the magnetization map is defined by the position and width of the maximum at $0 < \tau < \infty$. If the magnetization map has a larger dynamic range, $\Delta M_{2,2-6}(\tau_i)$ becomes broader and its maximum is located at higher frequency offset. These features are similar to that for the type-1 difference magnetization profiles. But this type of difference magnetization profiles can be acquired at transient conditions instead of the equilibrium conditions, which offers variable pulse duration for measurements.

Fig. 2(E) shows the type-3 difference magnetization profiles defined by Fig. 1. By subtraction of $M_e(\infty, \theta)$ from $M_e(0.025, \theta)$ obtained at RF amplitude of 2, 4 and 6 kHz, three difference magnetization profiles are generated as $\Delta M_{3,\omega_i} = M_e(0.025, \theta_i) - M_e(\infty, \theta_i)$ with ω_i of 2, 4 and 6 kHz. The subscript 3 denote the type-3 difference magnetization profile. At $\tau_R = 80$ ps, all three profiles have small amplitude located at the narrow region of the low offset, $\Delta M_{3,\omega_i} < 0.05$, in which the frequency offset and distribution vary as a function of ω_i. As τ_R increases, the amplitude of the profiles increases, i.e., $\Delta M_{3,\omega_i} \sim 0.35$ for $\tau_R = 1500$ ps and 0.45 for $\tau_R = 3000$ ps. This provides a simple method for spectral editing to completely suppress the short τ_R component without affecting the long τ_R component. The connection of this type of difference magnetization profile with the magnetization map is through three parameters, the width, the offset, and the amplitude of the profile. Thus, the larger dynamics range in the magnetization map, the wider distribution of larger amplitude, which is located at higher frequency offset. τ_1 and τ_2 can be chosen arbitrarily as long as $M_e(\tau_1, \theta) \gg M_e(\tau_2, \theta)$ is shown in the magnetization map. This type of difference magnetization profile permits to measure the magnetizations at low RF amplitudes and short pulse durations, thus the method can reduce the RF power depositions substantially.

In summary, magnetization map can be directly related to the dispersion of residual z-magnetization profiles and the pattern of the difference magnetization profiles. Three types of difference magnetization profiles can be used to identify the dynamics of paramagnetic ion chelates effectively. As stated early, the calculations in Fig. 2 are for paramagnetic ion chelates with $q = 1$ and $D = 3.16 \times 10^{-5}$ cm^2/s at 9.4 T. The magnetization maps, the equilibrium residual

z-magnetization profiles and three types of difference magnetization profiles generated by the numerical simulations can used to compare the effect of τ_R directly, which is the dynamic parameter of the inner shell water. This is the general situation for the paramagnetic agents in aqueous solutions, in which the contribution from the outer shell at $D = 3.16 \times 10^{-5}$ cm^2/s is small in comparing with the contribution from the inner shell that is directly proportional to τ_R^2. Thus, the magnetization map and the magnetization profiles are expected to change systematically as τ_R increases. Since the relaxation enhancement efficiency is a function of other factors such as the magnetic field strength B_0, the structural water number q, the diffusion coefficient D and multiple τ_R, the magnetization map are expected to be affected by these factors as well. In the next four sections, we will discuss their effects on the magnetization maps, as shown in the Fig. 3 below. The difference magnetization profiles corresponding to these maps can be easily generated in the same ways as those shown in Fig. 2 and will not be shown in the following discussions.

4.2. Effect of magnetic field strength B_0 on magnetization map

Magnetic field strength B_0 will affect the dynamic range of the magnetization map because $R_{1\rho}(\theta)/R_1$ and $R_{1\rho}(\theta)$ are a function of ω_H^2 [7]. Fig. 3(A) shows the magnetization maps for τ_R of 1500 ps, $D = 3.16 \times 10^{-5}$ cm^2/s at magnetic field strength of 4.7, 9.4 and 14.1 T. These calculated magnetizations only include the paramagnetic contribution. The dynamic range of the magnetization map is enhanced at the high field, because the relaxation enhancement efficiency $R_{1\rho}(\theta)/R_1$ increases as the magnetic field strength increases. But the rotating frame relaxation rate constant $R_{1\rho}(\theta)$ decreases slightly as the magnetic field strength increases [7]. Thus, the spins need a longer pulse duration τ to reach the equilibrium at high field, i.e., ~100 ms for 4.7 T, ~200 ms for 9.4 T and ~500 ms for 14.1 T. However, since the dynamic range is enhanced in off-resonance rotating frame, the same pulse duration τ can yield a much larger difference magnetization at higher field than that at lower field. Therefore, the increase of the magnetic field strength will enhance the capability of differentiating relaxivity for T_1/T_2-type paramagnetic agents and increase the sensitivity for detecting the dynamics of paramagnetic ion chelates.

4.3. Effect of coordinated water number q on magnetization map

The number of coordinated water in the inner shell will affect the magnetization map because both the relaxation enhancement efficiency $R_{1\rho}(\theta)/R_1$ and relaxation rate constant $R_{1\rho}(\theta)$ increase as q increases [7]. Fig. 3(B) shows the maps for Gd-DTPA with $\tau_R = 80$, 1500 and 3000 ps, $q = 3$, $D = 1.0 \times 10^{-6}$ cm^2/s at 9.4 T. These calculated magnetizations only include the paramagnetic contribution.

The hydration number is increased by a factor of 3 in comparing with the case shown in Fig. 2(A), the induced change in the magnetization map is dependent of τ_R. For $\tau_R = 80$ ps, the magnetization map is nearly the same as that for $q = 1$. In this case, the rotating frame relaxation rate constant $R_{1\rho}^{IS}(\theta)$ and the laboratory frame relaxation rate constant R_1^{IS} are tripled, but the relaxation enhancement efficiency $R_{1\rho}(\theta)/R_1 \sim 1$, which is the same as that for $q = 1$. Thus the magnetization map is not affected. For $\tau_R = 1500$ or 3000 ps, $R_{1\rho}^{IS}(\theta)$ and R_1^{IS} is directly proportional to q, but the increment for the relaxation enhancement efficiency $R_{1\rho}(\theta)/R_1$ is less than q times. Consequently, the dynamic range of the magnetization map is much larger and the pulse duration to reach the equilibrium is much shorter than that for $q = 1$. This effect is more predominant for $\tau_R = 3000$ ps than that for $\tau_R = 1500$ ps. In summary, a large hydration number q will increase the dynamic range of the magnetization map and the amplitude of the relaxivity. Both increments are proportional to the rotational correlation time. This relation permits to examine the smart paramagnetic labeling for which the change of hydration number q on the chelates highlights the progress of molecular events [26].

4.4. Effect of diffusion coefficient D on magnetization map

The dynamic environment of the paramagnetic ion chelates is related to the outer shell water by the diffusion coefficient D. This diffusion constant, as we pointed out in the previous paper, is the parameter that characterizes water motion within the immediate local vicinity of the paramagnetic relaxation center [7]. The alteration of $R_{1\rho}(\theta)/R_1$ as D decreases [7] will affect the magnetization map. Fig. 3(C) shows the map for Gd-DTPA at 9.4 T with $\tau_R = 80$, 1500 and 3000 ps, $q = 1$, $D = 1.0 \times 10^{-6}$ cm^2/s. These calculated magnetizations only include the paramagnetic contribution. The diffusion coefficient is decreased by a factor of 30 in comparing with the case in Fig. 2(A), the induced change in the magnetization map is dependent of τ_R. For $\tau_R = 80$ ps, the dynamic range of the magnetization map increases as the D decreases. For $\tau_R = 1500$ or 3000 ps, both the dynamic range of the magnetization map and the pulse duration τ to reach equilibrium are reduced. These are related to the alteration of the relaxation rate constants contributed from the outer shell water. For small τ_R such as single Gd-DTPA, the decrease of D will lead to the increase of $R_{1\rho}^{OS}(\theta)$ and R_1^{OS}. But the increment for $R_{1\rho}^{OS}(\theta)$ is larger than that for R_1^{OS}, which leads to $R_{1\rho}(\theta)/R_1 > 1$ and the increase of the dynamic range in the magnetization map. For large τ_R such as macromolecule conjugated Gd-DTPA, $R_{1\rho}^{IS}(\theta)$ generally is much larger than $R_{1\rho}^{OS}(\theta)$, but $R_1^{IS} \leqslant R_1^{OS}$. The increases of $R_{1\rho}^{OS}(\theta)$ and R_1^{OS} due to small D can generate a large denominator for the enhancement ratio, thus reduces the relaxation enhancement efficiency $R_{1\rho}(\theta)/R_1$. Consequently, the dynamic range of the magnetization map is reduced. On the other hand, $R_{1\rho}^{OS}(\theta)$ is increased at small D, which increases
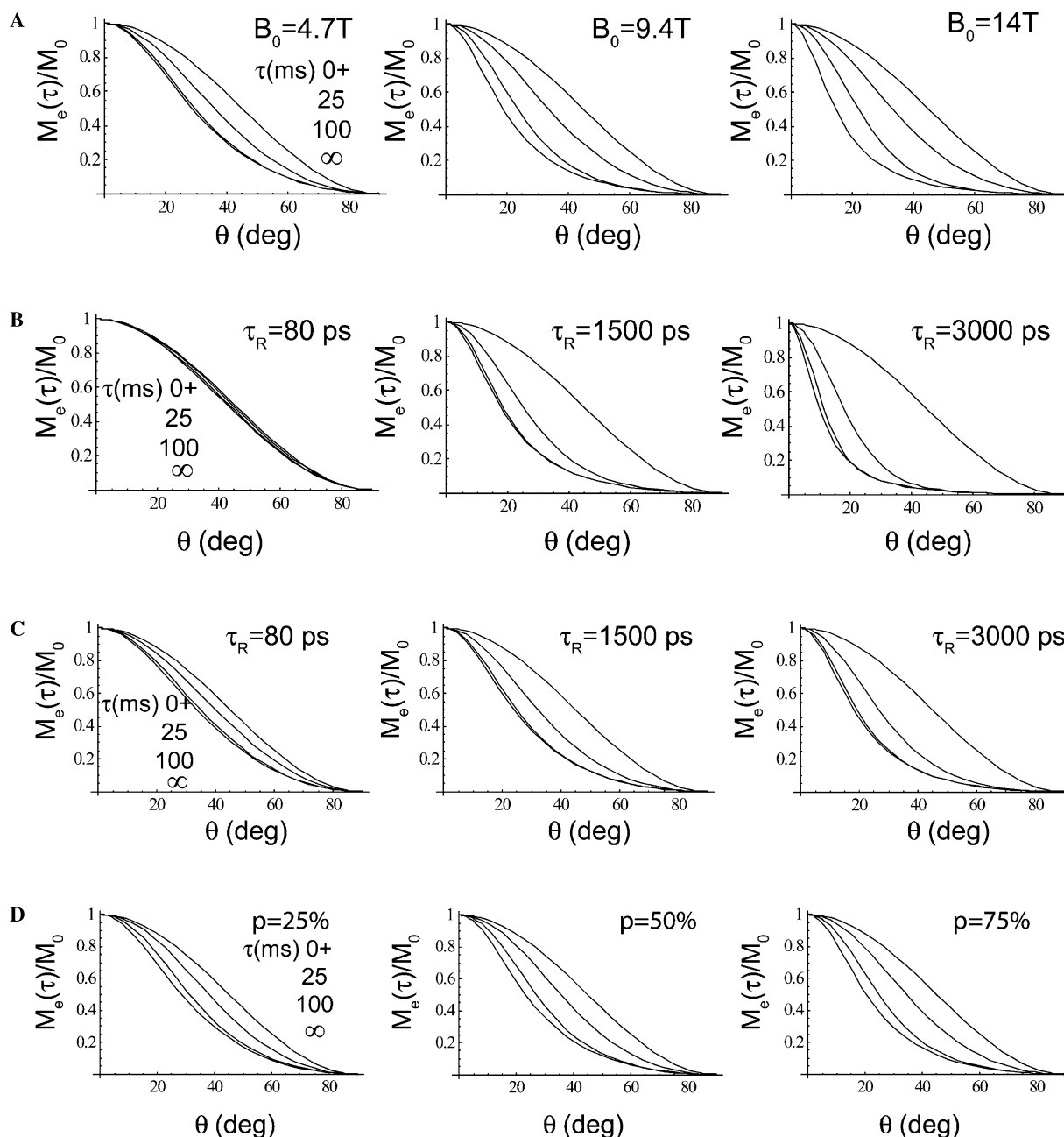
Fig. 3. Theoretically predicted magnetization maps for paramagnetic chelates in aqueous solutions as a function of various parameters. Molecular parameters are discussed in the text. (A) The dependence of magnetic field strength, $B_0 = 4.7$, 9.4 and 14.1 T. (B) The effect of high structural water number $q = 3$ at 9.4 T. (C) The effect of low diffusion coefficient $D = 1.0 \times 10^{-6}$ cm^2/s at 9.4 T. (D) The effect of mixing two components with τ_R of 80 ps and 1500 at 9.4 T. The mole fraction for the component with large τ_R is shown in the figure.

$R_{1\rho}(\theta)$ and leads to a decrease of τ to reach the equilibrium. Thus, the difference magnetization profiles as a function of pulse duration τ are quite different from that for large D in term of their frequency offset and distribution width. In summary, a small diffusion coefficient D will reduce the dynamic range of the magnetization map and increase the amplitude of relaxivity. Both changes depend on the rotational correlation time. This relation is very important for examining the paramagnetic agents in biological systems, where the local diffusion coefficient D is always much smaller than that in aqueous media. The magnetization

map can help to select RF parameters for experimental measurement and to assess the dynamics parameters for data analysis for these systems.

4.5. Effect of multiple rotational correlation time τ_R on magnetization map

Many biological systems may contain paramagnetic ion chelates with multiple τ_R such as the paramagnetic labeling which is bound to different sites. The magnetization maps for these systems will be the summation of the contributions

for each τ_R component, which will alter the overall relaxation rate constant and the overall relaxation enhancement efficiency. Since the coordinated water for the paramagnetic ion chelates is in fast exchange with the bulky water, the bulky water are relaxed as the competition of multiple relaxation pathways in the rotating frame. Here we consider a two-component system, where the residual magnetization is the sum of the contribution from the two components shown as follows:

$$M_e = \sum_{i=1}^{2} f_i M_{ei} \qquad (9)$$

where M_{ei} is the residual z-magnetization of the ith-component expressed by Eq. (5). f_i is the relaxation fraction of the ith-component, which is related to the mole fraction of the ith-component p_i and the rotating frame spin-relaxation rate constant of the ith-component $R_{1\rho,i}(\theta)$ as follows:

$$f_i = \frac{p_i R_{1\rho,i}(\theta)}{\sum_{j=1}^{2} p_j R_{1\rho,j}(\theta)}, \qquad (10)$$

$$p_i = 1 - \sum_{k=1}^{2} p_k. \qquad (11)$$

Fig. 3(D) shows the magnetization map for a two-component system, which contains a small τ_R component ($\tau_R = 80$ ps) and a large τ_R component ($\tau_R = 1500$ ps). These calculated magnetizations only include the paramagnetic contribution. The component fraction for the large τ_R component is 0.25, 0.5 and 0.75, respectively. The magnetization map is dominated by the features of the large τ_R component even with low mole fraction, and the dynamic range of magnetization map increases as the fraction of the large τ_R component increases. For a system contains more than two τ_R components, it is expected that the feature of the largest τ_R component will dominate the magnetization map. This relation can be used to explore paramagnetic labeling involved in the chemical equilibrium process of molecules events.

4.6. Experimental magnetization profiles for (Gd-DTPA)$_n$-macromolecules

Fig. 4(A) shows the residual z-magnetization profiles obtained at 9.4 T for Gd-DTPA attached to dextran, polylysine (PLS) and PAMAM-g5 dendrimer, their averaged molecular formula are: (Gd-DTPA)$_8$-dextran, (Gd-DTPA)$_{54}$-PLS and (Gd-DTPA-SCN-Bz)$_{41}$-PAMAM-g5. All macromolecule conjugated Gd-DTPA solutions used in this study have the diffusion coefficient D in the order of 10^{-5} cm^2/s [7], thus their inner shell relaxation rate constants dominate the total relaxation rate constants. These paramagnetic agents are used to confirm the dependence of the rotational correlation time τ_R predicted by the theoretical simulations shown in Fig. 2. Since the concentration of these macromolecules at 1 mM Gd(III) ranges from 0.12

to 0.018 mM, the magnetization transfer effect due to their slow tumbling motion can be neglected. Since the T_1 is shorter than 200 ms for these solutions and is longer than 2 s for the solvent, the diamagnetic contribution from the solvent can be neglected from their relaxation rate constants. Thus, the residual z-magnetization is directly related to the paramagnetic contribution and the simulated difference magnetization profiles shown in Fig. 2(A–E) can be used as reference for the dynamics of paramagnetic ion chelates.

Note that these macromolecules do not have molecular folding process as in the protein BSA. Thus, their chelates are assumed to have quite similar τ_R or an averaged τ_R, which is a function of the global tumbling motion time τ_g and the local reorientation motion time τ_i, $\tau_R^{-1} = \tau_g^{-1} + \tau_i^{-1}$. In principal, τ_R can be defined by accurate measurement of τ_g and τ_i via various strategies using high resolution NMR by site specific ^{13}C labeling of the chelates. For these paramagnetic agents, the τ_g and τ_i for the chelates has not been reported yet and the accurate measurement of these parameters is out the scope of this paper. But the mobility order of these paramagnetic agents can be predicted from their molecular structures as PLS ~ dextran > PAMAM-g5. The dendrimer PAMAM is less flexible than PLS and dextran. For the purpose of demonstrating the dependence of τ_R, a qualitative analysis of the trend in the difference magnetization profiles will be sufficient to support the theoretical predictions. Fig. 4(A) shows that the dispersion of the residual z-magnetization profiles for these paramagnetic agents is in the order of PLS < dextran < PAMAM-g5, which suggests that the averaged mobility of the chelates is PLS > dextran > PAMAM-g5.

Fig. 4(B) shows the type-1 difference magnetization profiles $\Delta M_{1,2–6}$, $\Delta M_{1,2–4}$ and $\Delta M_{1,4–6}$ generated from those shown in Fig. 4(A). As expected, the maximum of the difference magnetization profiles for PAMAM-g5-conjugated Gd-DTPA is substantially broader than that for other macromolecules, and its corresponding frequency offset is also shifted to higher frequency. The difference between the PLS-conjugated Gd-DTPA and dextran-conjugated Gd-DTPA is not substantially large but still distinguishable. For the difference magnetization profile $\Delta M_{1,2–6}$, the frequency offset of the maximum is found at 6 kHz for PLS-conjugated Gd-DTPA, 7 kHz for dextran-conjugated Gd-DTPA and 11 kHz for PAMAM-g5-conjugated Gd-DTPA; their half height width is 12, 15 and 30 kHz, respectively. The type-1 difference magnetization profiles are slightly broader than the theoretical patterns. But the dependence on τ_R is consistent with the predicted trend shown in Fig. 2(C). Their averaged τ_R are obtained from the difference magnetization profiles as PAMAM-g5 ~1.3 ns, dextran ~0.5 ns and PLS ~0.4 ns. Thus, type-1 difference magnetization profile can be used to differentiate paramagnetic ion chelates of different τ_R.

Fig. 4(C) shows the type-2 difference magnetization profiles $\Delta M_{2,2–6}(\tau_i)$ with $\tau_i = 0.025$ s, 0.1 s and ∞ for dextran-conjugated Gd-DTPA and PAMAM-g5-conjugated
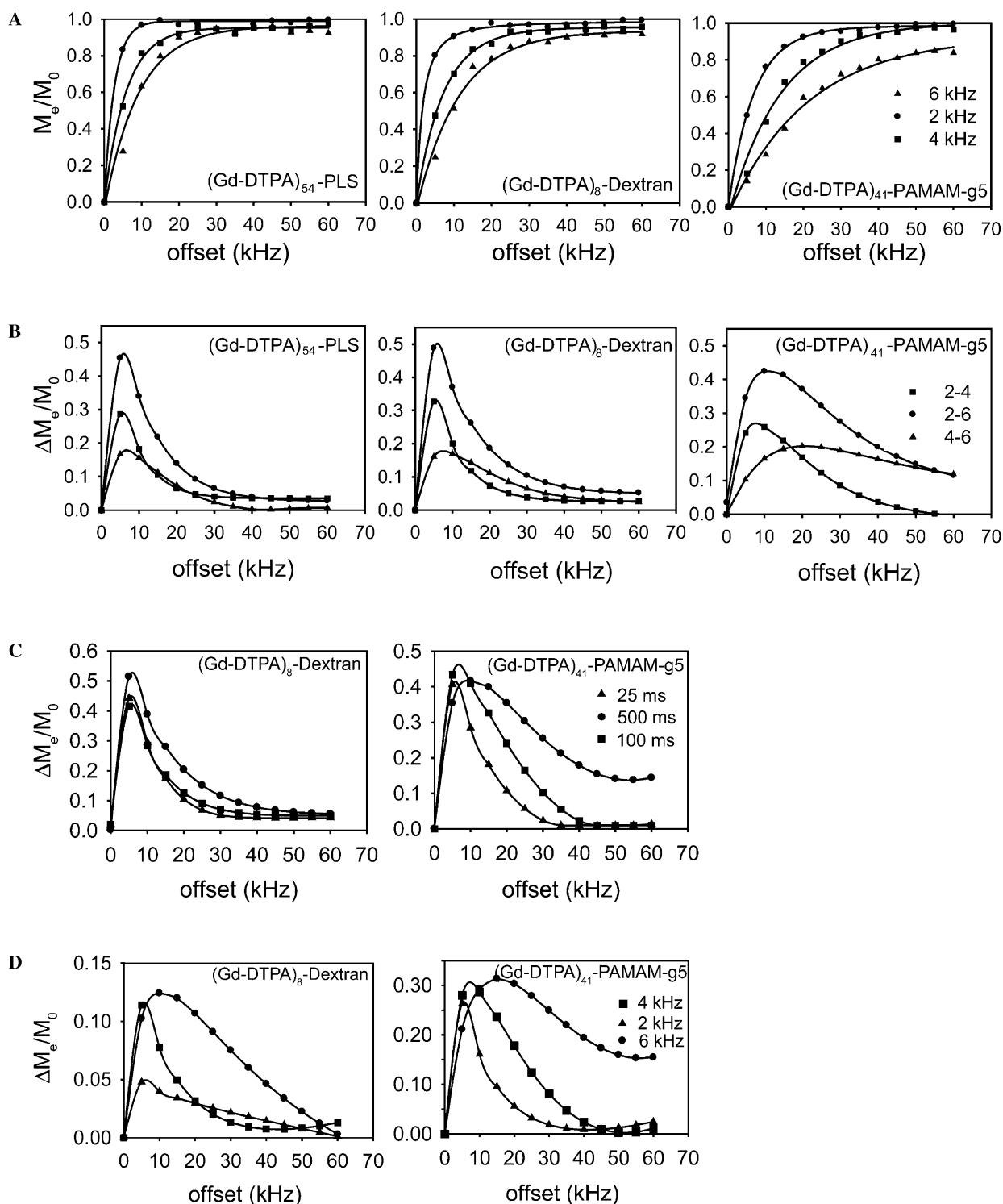
Fig. 4. Experimentally measured various magnetization profiles for aqueous $(Gd-DTPA)_n$-macromolecules at 1 mM Gd(III) at 9.4 T. (A) Residual z-magnetization profiles obtained with pulse duration of 500 ms and RF amplitude of 2, 4, 6 kHz. (B) Type-1 difference magnetization profiles, $\Delta M_{1,2-6}$, $\Delta M_{1,2-4}$ and $\Delta M_{1,4-6}$. (C) Type-2 difference magnetization profiles $\Delta M_{2,2-6}(\tau_i)$ with $\tau_i = 25$, 100 ms and ∞. (D) Type-3 difference magnetization profiles $\Delta M_{3,\omega_i}$ with $\omega_1 = 2$, 4 and 6 kHz.

Gd-DTPA. These two types of chelates have quite different τ_R as shown in Fig. 4(B). According to the numerical simulations shown in Fig. 2(C–E), the effect of τ_R will be reflected on all three types of difference magnetization profiles. For dextran-conjugated Gd-DTPA, the maximum of

$\Delta M_{2,2-6}(\tau_i)$ is located at nearly the same frequency offset ~6 or 7 kHz and the half height width increases slightly from 10 to 2 kHz as τ_i increases. For PAMAM-g5-conjugated Gd-DTPA, the maximum of $\Delta M_{2,2-6}(\tau_i)$ shifts to from 6 to 11 kHz as τ_i is increased. The half height width

becomes much broader, which is 10 kHz at 0.25 ms, 16 kHz at 100 ms and 30 kHz at the equilibrium. This confirms the theoretical prediction shown in Fig. 2(D) that the type-2 difference magnetization profiles can be used to identify τ_R. The experimental difference magnetization profiles were generated from the fitted residual z-magnetization profiles. The fitted curves may cause the experimental difference magnetization profiles slightly different from the theoretical simulations in some regions. Example as the intensities at the frequency offset larger than 40 kHz are slightly increased in Fig. 4(C), which may also appear in some difference magnetization profiles shown later. Since the increment is very small, this error will by the maxima located at much lower frequency offset.

Fig. 4(D) shows the type-3 difference magnetization profiles $\Delta M_{3,\omega_i} = M_e(0.025, \theta_i) - M_e(\infty, \theta_i)$ with $\omega_i = 2$, 4, 6 kHz for dextran-conjugated Gd-DTPA and PAMAM-g5-conjugated Gd-DTPA. In this case, for PAMAM-g5-conjugated Gd-DTPA the maximum of $\Delta M_{3,\omega_i}$ is located at the frequency offset of 6, 8 and 15 kHz as ω_i increases from 2 to 6 kHz. Their corresponding half-height widths are increased substantially, from 10, 20 to 40 kHz. The amplitude of these maxima is around 0.3, which is much larger than that ~0.12 for dextran-conjugated Gd-DTPA. For dextran-conjugated Gd-DTPA the maximum of $\Delta M_{3,\omega_i}$ is located at much lower frequency, which is 6 and 11 kHz for $\omega_i = 4$, 6 kHz. Their corresponding half-height width is much narrower, which is 9 and 27 kHz respectively. Because the difference between the residual z-magnetization profiles obtained at $\omega_i = 2$ kHz is too small thus the generated $\Delta M_{3,\omega_i}$ has much lower intensity than the theoretical predicted value. This situation may occur for $\tau_R \leqslant 0.5$ ns at 9.4 T. Except for this, the other two type-3 difference magnetization profiles are consistent with the theoretical simulations shown in Fig. 2(E), which suggests that type-3 difference magnetization profile can be used to differentiate the τ_R for paramagnetic ion chelates.

Thus, in agreed with the numerical simulations, all three types of difference magnetization profiles obtained experimentally demonstrate the dynamics difference for the macromolecules conjugated chelates. This suggests that any of these difference magnetization profiles can be used to efficiently differentiate the dynamics of paramagnetic ion chelates.

4.7. Experimental magnetization profiles for (Gd-DTPA)$_n$-BSA

Fig. 5(A) shows the residual z-magnetization profiles for aqueous (Gd-DTPA)$_n$-BSA at 1 mM Gd(III) at magnetic field strength of 4.7 or 9.4 T. The concentration of these macromolecules at 1 mM Gd(III) ranges from 0.17 to 0.034 mM. The magnetization transfer effect and the diamagnetic contribution from the solvent can be neglected. Because the molecular folding process, the attached chelates may have different τ_R, among which the chelate of larger τ_R will contribute more to the spin

relaxation than the others. Since the repulse force between the charged chelates, the number of chelates per BSA (n) is expected to affect the apparent τ_R. The comparison of $n = 6$ with $n = 30$ is used to probe the τ_R change induced by protein folding. The decrease of the number n of chelates induces interesting dispersion changes in the residual z-magnetization profiles. The dispersion of the residual z-magnetization profiles for $n = 6$ is larger than that for $n = 30$, as shown in Fig. 5(A). Their corresponding type-1 difference magnetization profiles are also different. The maximum of $\Delta M_{1,2-6}$ is at the frequency offset of 9 kHz with the half height width of 24 kHz for $n = 6$, which are 8 and 20 kHz for $n = 30$, respectively. This may attribute to that the attached Gd-DTPAs have net charges to generate repulsion force. Thus, the BSA is packed much tighter for $n = 6$ than that for $n = 30$, or the averaged τ_R for (Gd-DTPA)$_6$-BSA is slightly longer than that for (Gd-DTPA)$_{30}$-BSA. Such a small change can be demonstrated in the type-1 difference magnetization profiles, which suggests that this method can be used to examine the intra-molecular interaction by paramagnetic ion chelates.

The paramagnetic agents with $n = 30$ were measured at two magnetic field strengths to confirm the dependence of magnetic fields predicted by the theoretical simulations shown in Fig. 3(A). The dispersion of the residual z-magnetization profiles increases as the magnetic field strength changes from 4.7 to 9.4 T, which agrees with the theoretical predictions that $R_{1\rho}(\theta)/R_1$ is proportional to the square of proton Larmor frequency and the numerical simulations. Fig. 5(B) shows the type-1 difference magnetization profiles generated from the equilibrium magnetization profiles shown in Fig. 5(A). At 4.7 T, the maximum for $\Delta M_{1,2-6}$ is located at frequency offset of 7 kHz with the half height width of 16 kHz. At 9.4 T, the maximum is shifted to frequency offset of 8 kHz with the half height width of 20 kHz. These results agree with the theoretical predictions that the increase of B_0 will enhance the dynamic range of the magnetization map and that the type-1 difference magnetization profiles will have broader distributions with their maximum locating at higher offset.

4.8. Experimental magnetization profiles for Gd-DTPA mixing with (Gd-DTPA)$_6$-BSA

Fig. 6 shows the type-1 difference magnetization profiles obtained at 9.4 T for a series of two-component solutions. For these samples, the magnetization transfer effect and the diamagnetic contribution from the solvent can be neglected for the similar reasons as discussed above for the other samples. One component is Gd-DTPA, which has fast rotational motion, and the other one is (Gd-DTPA)$_6$-BSA, which has much slower dynamics than Gd-DTPA as known from above discussions. Since the Gd-DTPAs on the BSA are covalently bonded, there is no direct coupling between the Gd-DTPA and the (Gd-DTPA)$_6$-BSA.
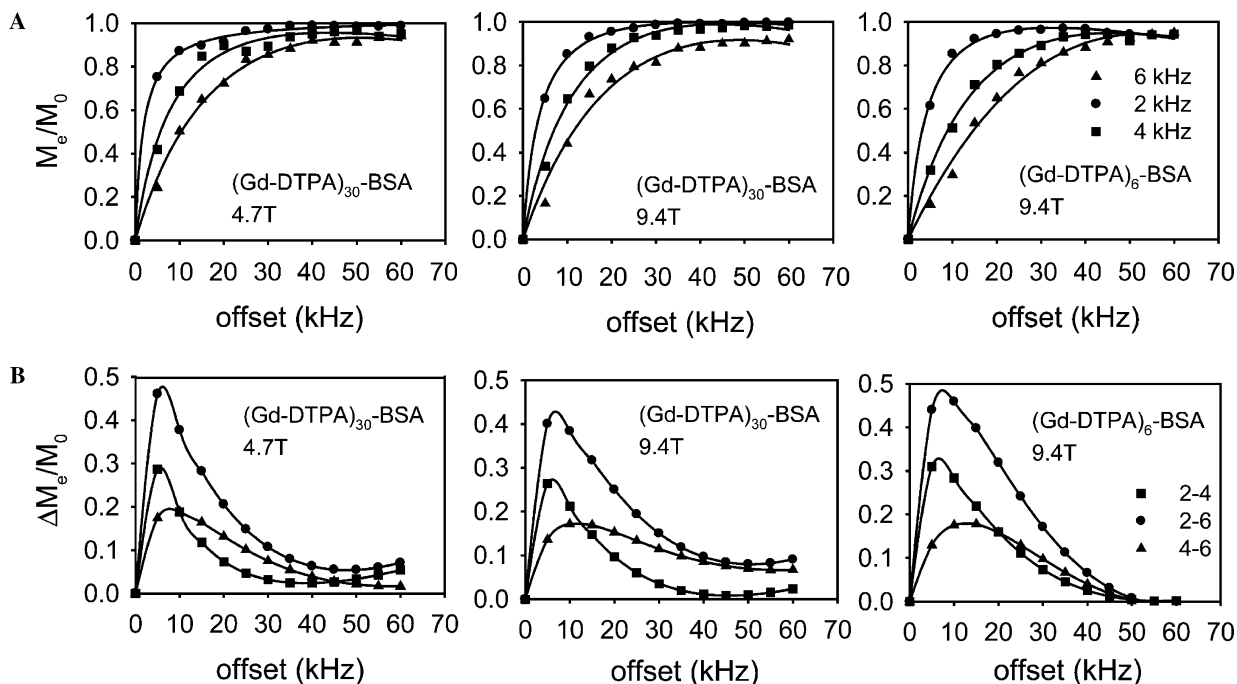
Fig. 5. Experimentally measured various magnetization profiles for aqueous (Gd-DTPA)$_n$-BSA ($n = 6, 30$) at 1 mM Gd(III) at 4.7 or 9.4 T. (A) Residual z-magnetization profiles acquired at pulse duration of 500 ms and RF amplitude of 2, 4 and 6 kHz. (B) Type-1 difference magnetization profiles, $\Delta M_{1,2\text{–}6}$, $\Delta M_{1,2\text{–}4}$ and $\Delta M_{1,4\text{–}6}$.
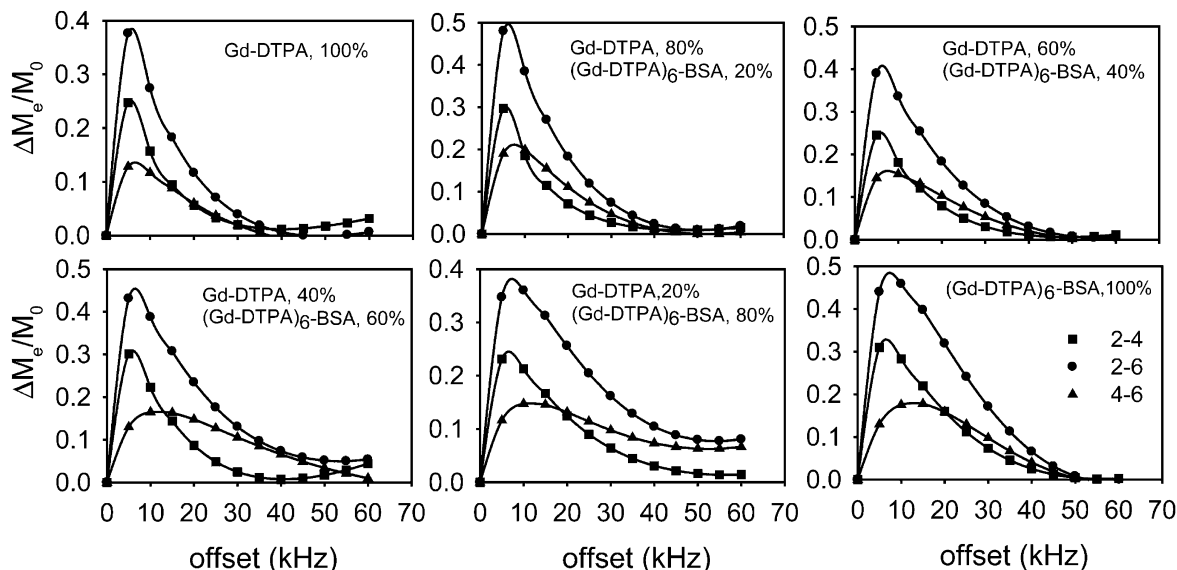

Fig. 6. Experimentally measured type-1 difference magnetization profiles for the mixed Gd-DTPA/(Gd-DTPA)$_6$-BSA solution at 1 mM Gd(III) at 9.4 T, $\Delta M_{1,2\text{–}6}$, $\Delta M_{1,2\text{–}4}$ and $\Delta M_{1,4\text{–}6}$. The mole fraction of (Gd-DTPA)$_6$-BSA is shown in the figure.

The τ_R is estimated to be 80 ps for the Gd-DTPA and ∼900 ps for the (Gd-DTPA)$_6$-BSA. These experiments are used to confirm the dependence of multiple τ_R. As the composition fraction of the (Gd-DTPA)$_6$-BSA increases, there is a systematic alteration of the type-1 difference magnetization profiles. The maximum of the distribution becomes broader with the frequency offset shifts to high offset, which suggests an increase of the observed τ_R. This result is consistent with the trend shown in the theoretically predicted magnetization maps in Fig. 3(D) that the increase of the large τ_R component fraction will enhance the dynamic range of the magnetization map.

5. Conclusions

A new method for determining the dynamics of paramagnetic ion chelates in aqueous solutions by off-resonance rotating frame technique has been developed.

In this method, a magnetization map is created for the residual z-magnetization of water in the off-resonance rotating frame by numerical simulations. Determined by the paramagnetic relaxation enhancement efficiency in the off-resonance rotating frame, the magnetization map is a function of the effective motional correlation time τ_c, diffusion coefficient D, hydration water number q and magnetic field strength B_0. Three types of difference magnetization profiles can be generated from the region of the magnetization map that is the most sensitive to the alteration of the enhancement efficiency, which are correlated with the effective motional correlation times through numerical simulations. By matching the experimental profiles with these theoretical simulations, the dynamics of the paramagnetic ion chelates in solutions can be directly identified. Experimental data for a series of macromolecule conjugated Gd-DTPA confirmed the theoretical predictions. Since the relaxation enhancement efficiency is proportional to the square of magnetic field strength, the dynamic range of the magnetization map will be increased as the field strength increases. Therefore, the magnetization map offers a unique high sensitive approach to access the dynamics of paramagnet ion chelates at high magnetic fields ($B_0 > 3$ T) where the relaxation in the traditional laboratory frame fails to differentiate them. Experimentally, the magnetization map can be used as guidance to select RF amplitudes or RF pulse durations, which is extremely important for *in vivo* applications which always require the RF power depositions within the safety guideline. Since the dynamics range of the magnetization map reflects the relaxation enhancement efficiency in the off-resonance rotating frame, the method not only can determine the dynamics for T_1-type paramagnetic agents but also can evaluate the relaxation enhancement efficiency for T_2-type paramagnetic agents [7]. We will demonstrate in a successive paper, this method will be very useful for the dynamics of paramagnetic ion chelates in the presence of strong magnetization transfer effect. Thus, it will be a powerful tool in detecting the dynamic of paramagnetic labeling *in vivo*.

Acknowledgment

Appendix A

We provide here the rotating frame spin–lattice relaxation rate constants for the inner shell water $R_{1\rho}^{IS}(\theta)$ and for the outer shell of water $R_{1\rho}^{OS}(\theta)$ that are used in Eq. (7). The detailed derivations for these parameters have been originally described in the previous paper [7].

The rotating frame spin–lattice relaxation rate constant for inner shell water is as follows:

$$R_{1\rho}^{IS}(\theta) = \frac{P_M q}{1/R_{1\rho,d}(\theta) + \tau_m} \tag{A.1}$$

where P_M is the molar fraction of metal ion, q is the number of water molecular bound per metal ion, τ_m is the residual life time of the bound water. $R_{1\rho,d}(\theta)$ is the rotating frame spin–lattice relaxation rate constant caused by electron-dipolar coupling interaction and is expressed as follows:

$$\begin{aligned}
R_{1\rho,d}(\theta) = K\{ &2\sin^2\theta J(\omega_e) + \sin^4(\theta/2)J(\omega_S - \omega_H + \omega_e) \\
&+ \cos^4(\theta/2)J(\omega_S - \omega_H - \omega_e) \\
&+ 3\cos^4(\theta/2)J(\omega_H + \omega_e) + 3\sin^4(\theta/2)J(\omega_H - \omega_e) \\
&+ 3/2\sin^2\theta(J(\omega_S + \omega_e) + J(\omega_S - \omega_e)) \\
&+ 6\cos^4(\theta/2)J(\omega_S + \omega_H + \omega_e) + 6\sin^4(\theta/2) \\
&\times J(\omega_S + \omega_H - \omega_e)\}.
\end{aligned} \tag{A.2}$$

At the high magnetic field, $\omega_S \gg \omega_H \gg \omega_e$, $R_{1\rho,d}(\theta)$ can be simplified as

$$R_{1\rho,d}(\theta) \sim K\{2f_1(\theta)J(\omega_e) + 3f_2(\theta)J(\omega_H)\}. \tag{A.3}$$

In this formalism,

$$K = \frac{2}{15}\frac{\gamma_H^2\gamma_S^2\hbar^2 S(S+1)}{r^6},$$
$$f_1(\theta) = \sin^2(\theta),$$
$$f_2(\theta) = \sin^4(\theta/2) + \cos^4(\theta/2),$$
$$J(\omega) = \frac{\tau_c}{1 + \omega^2\tau_c^2},$$
$$\tau_c^{-1} = \tau_R^{-1} + \tau_m^{-1} + T_{1e}^{-1}$$
$$T_{1e}^{-1} = \frac{1}{5\tau_{S0}}\left[\frac{1}{1 + \omega_S^2\tau_v^2} + \frac{4}{1 + 4\omega_S^2\tau_v^2}\right],$$

where θ is the angle for the effective field, τ_v is the correlation time characterizing the fluctuation of the zero field splitting (ZFS) and τ_{S0} is related to ZFS constant B as $\tau_{S0} = \tau_v/5B$. For macromolecule conjugated paramagnetic chelates, τ_m is the residual time of structural water, T_{1e} is electronic relaxation time. τ_R is the rotational correlation time, which is a sum of contributions from internal reorientation motion (τ_i) and global tumbling motion (τ_g) and $\tau_R^{-1} = \tau_i^{-1} + \tau_g^{-1}$.

The rotating frame spin–lattice relaxation rate constant for the outer shell $R_{1\rho}^{OS}(\theta)$ is expressed as,

$$\begin{aligned}
R_{1\rho}^{OS}(\theta) = K'\{ &2f_1(\theta)\left(1 + \alpha B_S^2(x)\right)J_{1OS}(\omega_e) + 3f_2(\theta) \\
&\left[(1 + \alpha)B_S^2(x)J_{1OS}(\omega_H, \tau_D, T_{1e} \to \infty)\right. \\
&\left.+ \left(1 - B_S^2(x)\right)J_{1OS}(\omega_H, \tau_D, T_{1e})\right]\}
\end{aligned} \tag{A.4}$$

with

$$K' = \frac{32\pi}{405}\hbar^2\gamma_H^2\gamma_S^2 S(S+1)\frac{N_A}{1000}\left(\frac{C}{dD}\right),$$

$$J_{1OS}(\omega_H, \tau_D, T_{1e}) = \text{Re}\left(\frac{1 + (1/4)(i\omega\tau_D + \tau_D/T_{1e})}{1 + (i\omega\tau_D + \tau_D/T_1)^{1/2} + (4/9)(i\omega\tau_D + \tau_D/T_{1e}) + (1/9)(i\omega\tau_D + \tau_D/T_{1e})^{3/2}}\right),$$

$$\tau_D = d^2/D$$

$$B_S(x) = \left(\frac{2S+1}{2S}\right)\coth\left[\left(\frac{2S+1}{2S}\right)x\right] - \left(\frac{1}{2S}\right)\coth\left[\frac{x}{2S}\right],$$

where $x = \mu B_0/RT$, $\alpha = (2S-1)/(S+1)$, μ is the magnetic moment of metal ion, $\mu = \gamma_S \hbar S$, N_A is the number of metal ion per cubic centimeter, d is the distance of closet approach of the water to the metal complex, τ_D is the relative translation diffusion time, $\tau_D = d^2/3(D_H + D_S)$, D_H and D_S are the diffusion coefficients of water and metal ion.

The laboratory frame spin–lattice relaxation rate constants R_1^{IS} and R_1^{OS} can be derived by setting $\theta = 0$, or found elsewhere [7,5,20,21].

References

[1] S.H. Koenig, R.D. Brown III, Relaxometry of magnetic resonance imaging contrast agents, Magn. Reson. Annu. (1987) 263–286.

[2] S.H. Koenig, R.D. Brown III, Field-cycling relaxometry of protein solutions and tissue: implications for MRI, Progr. NMR Spectrosc. 22 (1990) 487–567.

[3] R.B. Lauffer, T.J. Brady, R.D. Brown III, C. Baglin, S.H. Koenig, 1/T1 NMRD profiles of solutions of Mn^{2+} and Gd^{3+} protein-chelate conjugates, Magn. Reson. Med. 3 (1986) 541–548.

[4] D.R. Bruton, S. Forsen, G. Karlstrom, Proton Relaxation enhancement (PRE) in biochemistry: a critical survey, Progr. NMR Spectrosc. 13 (1979) 1–45.

[5] R.B. Lauffer, Paramagnetic metal complexes as water proton relaxation agents for NMR imaging: theory and design, Chem. Rev. 87 (1987) 901–927.

[6] R. Weissleder, U. Mahmood, Molecular imaging, Radiology 219 (2001) 316–333.

[7] H. Zhang, Y. Xie, Efficiency of paramagnetic relaxation enhancement in off-resonance rotating frame, J. Magn. Reson. 181 (2006) 212–222.

[8] P.J. Keller, W.W. Hunter Jr., P. Schmalbrock, Multisection fat-water imaging with chemical shift selective presaturation, Radiology 164 (1987) 539–541.

[9] S.D. Wolff, R.S. Balaban, Magnetization transfer contrast (MTC) and tissue water proton relaxation in vivo, Magn. Reson. Med. 10 (1989) 135–144.

[10] T.L. James, G.B. Matson, I.D. Kuntz, R.W. Fisher, Rotating frame spin–lattice relaxation in the presence of an off-resonance radio frequency field. Investigation of intermediate molecular motions, J. Magn. Reson. 28 (1977) 417–426.

[11] T.L. James, G.B. Matson, I.D. Kuntz, Protein rotational correlation times determined in aqueous solution by carbon-13 rotating frame spin–lattice relaxation in the presence of an off-resonance radiofrequency field, J. Am. Chem. Soc. 100 (1978) 3590–3594.

[12] T. Schleich, C.F. Morgan, G.H. Caines, Protein rotational correlation times by carbon-13 rotating-frame spin–lattice relaxation in presence of off-resonance radiofrequency field, Methods Enzymol. 176 (1989) 386–418.

[13] C.F. Morgan, T. Schleich, G.B. Caines, Assessment of protein reorientational diffusion in solution by ^{13}C off-resonance rotating frame spin–lattice relaxation: effect of polydispersity, Biopolymers 29 (1990) 501–507.

[14] J.M. Rydzewski, T. Schleich, Deuterium off-resonance rotating frame spin–lattice relaxation of macromolecular bound ligands, Biophys. J. 70 (1996) 472–1484.

[15] Z. Luz, S.S. Meiboom, Proton relaxation in dilute solutions of cobalt(II) and nickel(II) ions in methanol and the rate of methanol exchange of the solvation sphere, J. Chem. Phys. 40 (1964) 2686–2692.

[16] T.J. Swift, R.E. Connick, NMR-relaxation mechanisms of O^{17} in aqueous solutions of paramagnetic cations and the lifetime of water molecules in the first coordination sphere, J. Chem. Phys. 37 (1962) 307–320.

[17] G. Lipari, A. Szabo, Model-free approach to the interpretation of nuclear magnetic resonance relaxation in macromolecules. 1. Theory and range of validity, J. Am. Chem. Soc. 104 (1982) 4546–4559.

[18] J. Freed, Dynamic effects of pair correlation functions on spin relaxation by translational diffusion in liquids. II. Finite jumps and independent T1 processes, J. Chem. Phys. 68 (1978) 4034–4037.

[19] R. Regatte, S.V.S. Akella, A.J. Wheaton, A. Borthakur, J.B. Kneeland, R. Reddy, $T_{1\rho}$-relaxation mapping of human femoral-tibial cartilage in vivo, J. Magn. Reson. Imag. 18 (2003) 336–341.

[20] P. Caravan, J.J. Ellison, T.J. McMurry, R.B. Lauffer, Gadolinium(III) chelates as MRI contrast agents: structure, dynamics, and applications, Chem. Rev. 99 (1999) 2293–2352.

[21] K.E. Kellar, P.M. Henrichs, M. Spiller, S.H. Koenig, Relaxation of solvent proton by solute Gd^{3+}-chelates revisited, Magn. Reson. Med. 37 (1997) 730–735.

[22] P.F. Sieving, A.D. Watson, S.M. Rockage, Preparation and characterization of paramagnetic polychelates and their protein conjugates, Bioconjug. Chem. 1 (1990) 65–71.

[23] L.H. Bryant Jr., M.W. Brechbiel, C. Wu, J.W.M. Bulte, V. Herynek, J.A. Frank, Synthesis and relaxometry of high-generation (G = 5,7,9, and 10) PAMAM dendrimer-DOTA-gadolinium chelates, J. Magn. Reson. Imag. 9 (1999) 348–352.

[24] F.E. Armitage, D.E. Richardson, K.C.P. Li, Polymeric contrast agents for magnetic resonance imaging: synthesis and characterization of gadolinium diethylenetriaminepentaacetic acid conjugated to polysaccharides, Bioconjug. Chem. 1 (1990) 365–374.

[25] E.C. Wiener, M.W. Brechbiel, H. Brothers, R.L. Magin, O.A. Gansow, D.A. Tomalia, P.C. Lauterbur, Dendrimer-based metal chelates: a new class of magnetic resonance imaging contrast agents, Magn. Reson. Med. 31 (1994) 1–8.

[26] A.Y. Louie, M.M. Huber, E.T. Ahrens, U. Rothbacher, R. Moats, R.E. Jacobs, S.E. Fraser, T.J. Meade, In vivo visualization of gene expression using magnetic resonance imaging, Nat. Biotechnol. 18 (2000) 321–325.